Tailored Surface-Enhanced Raman Nanopillar Arrays Fabricated by Laser-Assisted Replication for Biomolecular Detection Using Organic Semiconductor Lasers

Xin Liu,[*,†,§] Sergei Lebedkin,[⊥] Heino Besser,[∥,#] Wilhelm Pfleging,[∥,#] Stephan Prinz,[†,⊗] Markus Wissmann,[§,#] Patrick M. Schwab,[†,§] Irina Nazarenko,[∇] Markus Guttmann,[§,#] Manfred M. Kappes,[⊥,‡] and Uli Lemmer[*,†,§]

[†]Light Technology Institute (LTI) and [‡]Institute of Physical Chemistry (IPC), Karlsruhe Institute of Technology, 76128 Karlsruhe, Germany, [§]Institute of Microstructure Technology (IMT), [⊥]Institute of Nanotechnology (INT) and [∥]Institute for Applied Materials — Applied Materials Physics (IAM-AWP), Karlsruhe Institute of Technology, 76344 Eggenstein-Leopoldshafen, Germany, [#]Karlsruhe Nano Micro Facility (KNMF), 76344 Eggenstein-Leopoldshafen, Germany, and [∇]Institute for Environmental Health Sciences and Hospital Infection Control, Medical Center-University of Freiburg, 79106 Freiburg, Germany [⊗]Present address: TRUMPF Scientific Lasers GmbH + Co. KG, 85774 Unterföhring-München, Germany.

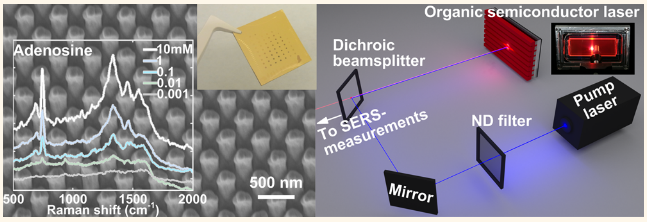

ABSTRACT Organic semiconductor distributed feedback (DFB) lasers are of interest as external or chip-integrated excitation sources in the visible spectral range for miniaturized Raman-on-chip biomolecular detection systems. However, the inherently limited excitation power of such lasers as well as oftentimes low analyte concentrations requires efficient Raman detection schemes. We present an approach using surface-enhanced Raman scattering (SERS) substrates, which has the potential to significantly improve the sensitivity of on-chip Raman detection systems. Instead of lithographically fabricated Au/Ag-coated periodic nanostructures on Si/SiO$_2$ wafers, which can provide large SERS enhancements but are expensive and time-consuming to fabricate, we use low-cost and large-area SERS substrates made *via* laser-assisted nanoreplication. These substrates comprise gold-coated cyclic olefin copolymer (COC) nanopillar arrays, which show an estimated SERS enhancement factor of up to ~10^7. The effect of the nanopillar diameter (60–260 nm) and interpillar spacing (10–190 nm) on the local electromagnetic field enhancement is studied by finite-difference-time-domain (FDTD) modeling. The favorable SERS detection capability of this setup is verified by using rhodamine 6G and adenosine as analytes and an organic semiconductor DFB laser with an emission wavelength of 631.4 nm as the external fiber-coupled excitation source.

KEYWORDS: Raman spectroscopy · surface-enhanced Raman scattering · nanostructure fabrication · nanoimprint lithography · laser material processing · organic semiconductor distributed-feedback lasers

Raman spectroscopy is an ideal label-free optical detection technique that can provide rich information on the molecular structure and composition of analytes, based on their vibrational fingerprints.[1−3] For analysis of aqueous solutions, for instance in life science, Raman detection has an important advantage over infrared or near-infrared absorption, namely, practically no perturbing signal from water.[4−6] Combined with microfluidic techniques, Raman spectroscopy is promising for biomolecular detection in a miniaturized lab-on-a-chip (LOC) device.[7−10] For this Raman-on-chip approach, either an external, *e.g.*, fiber-coupled, or a chip-integrated laser source can be used. Organic semiconductor lasers (OSLs) are of particular interest as they are miniature emitters covering the whole visible spectral range.[11−15] Very low laser thresholds have been demonstrated, and these lasers can even be pumped with microsized light-emitting diodes.[16] Furthermore, they can be integrated into LOCs by shadow mask[17] and printing techniques.[18] Narrow line width (required for Raman spectroscopy) and single longitudinal mode lasing can be realized using distributed

* Address correspondence to
uli.lemmer@kit.edu,
xin.liu@kit.edu.

Received for review August 12, 2014
and accepted December 16, 2014.

10.1021/nn506589a

feedback (DFB) laser structures.[19−21] In general, the integration of high power laser sources into lab-on-a-chip devices is challenging. This is not an issue for OSLs that have a typical power level of less than 1 mW. Recently, we have demonstrated the application of organic semiconductor DFB lasers (DFB-OSLs) as excitation sources for Raman measurements of sulfur and cadmium sulfide powders.[22,23] Although a low average power of the OSL (∼0.2 mW) was used in these measurements, the large Raman scattering efficiencies of the analytes enabled a straightforward Raman band detection. In the case of biomolecular analytes, the smaller Raman scattering cross sections, the limited excitation power of LOCs, as well as typically low concentrations of analytes would lead to very small or undetectable Raman signals under comparable excitation/detection conditions. A promising approach for overcoming this challenge is to use surface-enhanced Raman scattering (SERS) effect thus greatly increasing the Raman signal.

SERS occurs mainly due to a plasmonic effect in metallic nanostructures. Specifically, irradiation produces very high local electric field which leads to enhanced Raman scattering from molecules adsorbed on or near the metallic nanostructures.[24−26] Raman enhancement factors of up to $\sim10^{11}$, sufficient for a single-molecule detection, have been demonstrated in SERS "hot spots" (regions of the highest local electric field) associated with silver and gold colloids or in junctions between metal nanoparticles.[27,28] High Raman enhancement factors have also been demonstrated for individual nanostructured particles such as nanoshells,[29] nanostars[30] and anisotropically etched octahedrals.[31] However, practical SERS substrates composed of these nanostructured particles, which are typically assembled by random aggregation,[32] still lack uniformity and reproducibility in enhancement factor.[33] A compromise between moderate enhancement and high reproducibility can be offered by periodic nanostructures, which can be realized by advanced nanopatterning and deposition techniques such as nanosphere lithography[34] and physical vapor evaporation.[35] The uniformly patterned periodic nanodome and nanopillar metallic/silicon structures have demonstrated "hot spot" SERS enhancement factors of up to $\sim10^8$ on active substrates.[36−40]

Several techniques to fabricate periodic nanostructures are available. Electron beam lithography (EBL) offers maximum control over the nanostructures but suffers from low throughput and high costs. On the other hand, nanosphere lithography does not provide complete control over resulting nanostructure morphologies. Both methods cannot easily be integrated into the LOC fabrication. These problems can be solved through nanoimprint lithography (NIL) using a patterned silicon wafer as a reusable molding template. A subsequent gold coating is the only fabrication step requiring high vacuum. Several NIL techniques have been employed for the fabrication of SERS substrates. These include soft lithography,[41] UV-assisted NIL,[42] and thermal NIL (also known as hot embossing).[43] It is mandatory to use specific elastomeric materials in the soft-lithography and special photoactive materials in the UV-NIL process. These limitations would severely constrain the fabrication of SERS LOC systems. In contrast, thermal NIL is advantageous for parallel replication onto a common polymer substrate. Nevertheless, the local fabrication of nanostructures on predetermined chip sites is very difficult. Furthermore, the large-area and long-time heating can be detrimental for existing LOC microfluidic channels or other preexisting photonic elements. As we demonstrate below, these limitations can be overcome by fabricating SERS-active substrates by laser-assisted replication process[44] using a scanning laser beam from a high-power near-infrared CW laser diode.

Therefore, SERS nanopillar substrates were fabricated by laser-assisted replication and subsequent gold-film deposition. The method provides replication accuracy down to ∼20 nm. Several different nanopillar arrays have been prepared in order to study the effect of nanopillar diameter and spacing on the Raman enhancement factor. The latter is estimated to be $\sim10^7$ for the optimum nanopillar arrangement when using rhodamine 6G as the analyte. The experimental results are supported by finite-difference-time-domain (FDTD) simulations of the local electromagnetic field distribution modified by the nanopillar arrays. Finally, we demonstrate sensitive Raman detection of adenosine drop-cast onto optimized SERS nanopillar arrays from aqueous solution using an organic semiconductor DFB laser as an excitation source.

RESULTS AND DISCUSSION

We used EBL for fabrication of the silicon templates containing several sites with different patterns of inverted nanopillar (nanowell) arrays, each taking up an area of 0.5 × 0.5 mm^2. Figures S1, S2 (Supporting Information) show a schematic illustration of the fabrication process and nanostructure details of one representative silicon template. A schematic illustration of the subsequent laser-assisted replication process is depicted in Figure 1a. In comparison with common polymer substrate materials, like polydimethylsiloxane (PDMS) or poly(methyl methacrylate) (PMMA), cyclic olefin copolymer (COC) demonstrates relatively weak Raman signals, *i.e.*, weak interference with analyte signals[45,46] and therefore it was chosen to build SERS nanopillar arrays. A 1 mm-thick COC substrate with a size of 20 × 20 mm^2 was positioned on the template, covered with a glass plate (thus providing a contact pressure of ∼0.1 MPa) and exposed to the laser diode beam (50 W at 940 nm). The laser was focused to a ∼ 0.3 mm^2 spot and scanned the COC substrate with a

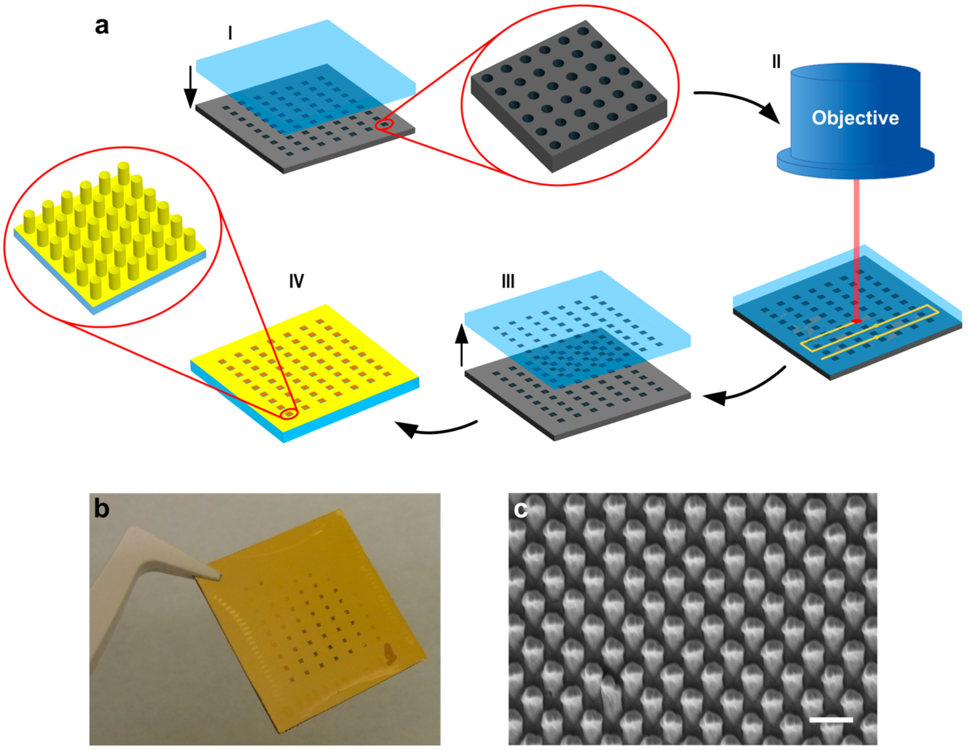

Figure 1. (a) Schematic illustration of the laser-assisted replication process: (I) positioning of the COC substrate on a patterned silicon template, (II) laser-assisted replication, (III) detachment of the substrate and (IV) sputter-deposition of a thin gold-layer. (b) Photograph of a gold-coated COC SERS substrate with 7 × 9 active nanopillar array sites. (c) SEM image of one active SERS site with nanopillars having a diameter of 200 nm and a spacing of 190 nm. The scale bar corresponds to 500 nm.

velocity up to 40 mm/s. Since the COC is transparent for the applied laser wavelength, the laser beam was mainly absorbed by the silicon surface in contact with the COC substrate. The laser scanning parameters were adjusted so that the local temperature of the irradiated polymer region was increased to exceed its glass transition temperature $T_g \sim 140$ °C. Above T_g the nanostructures on the rigid template were (inversely) replicated into the polymer substrate. The laser-assisted replication took about 8 min for one 20×20 mm^2 polymer chip. After cooling down, the polymer substrate with positively replicated nanostructures was detached from the silicon template and the process was repeated with a fresh COC substrate. No degradation of the silicon stamps was observed after more than five replications. A final gold sputter deposition completed the fabrication of a SERS-active substrate. Figure 1b presents a photograph of the completed SERS nanopillar array chip fabricated on a COC substrate comprising 7 × 9 nanopillar array sites. The contrast variance indicates different nanopillar patterns. The scanning electron microscope (SEM) image of one representative SERS nanopillar array site illustrates nearly defect-free replication (see Figure 1c). A stringent inspection of SEM images revealed that typically ∼2−10% and rarely up to 30% of all nanopillars were slightly bent, deformed or shifted. However, we expect only little influence on the overall SERS performance of nanopillar arrays by these minor shape-defects.

It is well-known that the characteristic size of nanostructures and spacing between them in a periodic array can dramatically influence the SERS enhancement factors. In order to investigate the effect of both, we fabricated different patterns of Au/COC nanopillars with diameter *D*, varying from 60 to 260 nm in steps of 20 nm. With regard to the feasible EBL resolution and replication accuracy, the minimum spacing between adjacent COC nanopillars was set at 20 nm. The typical thickness of deposited gold-films was measured to be about 25 nm on the top and 5 nm on the side walls of the nanopillars, respectively. Correspondingly, the minimum spacing between Au/COC pillars was $d \sim 10$ nm. In addition, we fabricated arrays with larger interpillar spacing, *e.g.*, $d = 190$ nm and $d = D$, *i.e.*, of the same value as diameter *D*. Figure 2 shows SEM and atomic force microscope (AFM) images of three SERS nanopillar arrays with $D = 100$ nm and different interpillar spacings. The height of the COC nanopillars in all arrays was about 80 nm.

The main SERS enhancement mechanisms have been proposed to be of electromagnetic and chemical origin.[47] In our case, the SERS effect arises mainly because the nanosized gap between nanopillars is associated with an intense localized electromagnetic field. Indeed, a metallic nanopillar array can be considered as an array of optical antennas.[48] The induced localized surface plasmon resonance (LSPR) effect contributes to the enhancement both of the incident

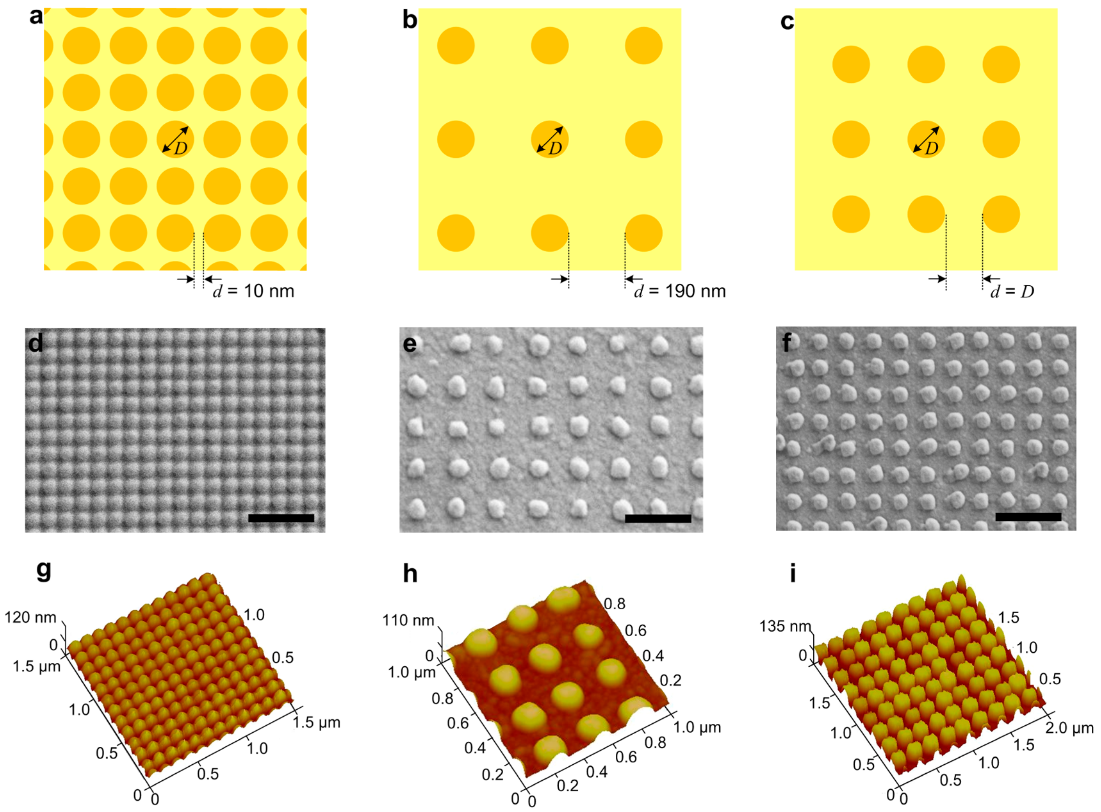

Figure 2. (a−c) Schemes of nanopillar arrays with interpillar spacing $d = 10$ nm, $d = 190$ nm and $d = D$ where D is the nanopillar diameter. (d−f) SEM images of the gold-coated COC nanopillar arrays with $D = 100$ nm and $d = 10$, 190, and 100 nm, respectively. The scale bars correspond to 500 nm. (g−i) Corresponding AFM images of the gold-coated COC arrays of nanopillars.

excitation and Raman scattered light.[48] The local SERS electromagnetic enhancement factor (EF) scales approximately as[47]

$$\mathrm{EF} \propto \frac{|E|^4}{|E_0|^4} \qquad (1)$$

where $|E|$ is the amplitude of the enhanced local electric field and $|E_0|$ is the amplitude of incoming electromagnetic wave.

The surface plasmon resonance behavior of the Au/COC nanopillars was first characterized by measuring their scattering properties with white-light illumination dark-field microscopy (for details see Materials and Methods and Figures S3 in Supporting Information).[49] The measurements also indicate a strong resonant enhancement at wavelength around 650 nm. For a spacing of $d = 10$ nm, the nanopillar resonance is found to be dependent on the nanopillar diameter D. The scattering peaks shift toward longer wavelengths for larger nanostructures and the peak intensities increase for larger nanostructures, as shown in Figure S3b (Supporting Information). To elucidate the electromagnetic field distribution on the active SERS-substrates, we used the FDTD method to simulate the near-field electric field distribution in modeled Au/COC nanopillar arrays excited with a normally incident plane wave at $\lambda = 632.8$ nm, polarized along the x-axis (as applied in the experiment). In this modeling we assume a 25 nm-thick gold-layer on top of the 80 nm-high COC nanopillars and a 5 nm-thick gold-layer on their side walls, as shown in Figure 3a (for simulation details see Materials and Methods and Figures S4−S6 in Supporting Information). The simulation results for nanopillars with a diameter $D = 100$ nm and three different interpillar spacings are shown in Figure 3b−d with the color-coded intensity representing the normalized amplitude of the enhanced electric field $|E|$ with respect to the amplitude of the incoming electric field $|E_0|$. For nanopillars with the spacing of 10 nm, the enhanced electric field regions with two antinodes are clearly seen within the gaps between adjacent nanopillars (see Figure 3b). This minimum spacing also offered the highest electric field enhancement, as could be expected due to the surface plasmon coupling effect.[47] When the spacing exceeded ∼30 nm, the major electric field enhancement could only be found in the vicinity of nanopillar side walls, indicating a weakened electromagnetic coupling between nanopillars, as shown in Figure 3c,d.

Furthermore, enhanced field regions were also found to be generated inside nanopillars and thus "inaccessible" for SERS of analyte molecules. When the nanopillar diameter exceeded ∼180 nm and the interpillar spacing was similarly large, the enhanced

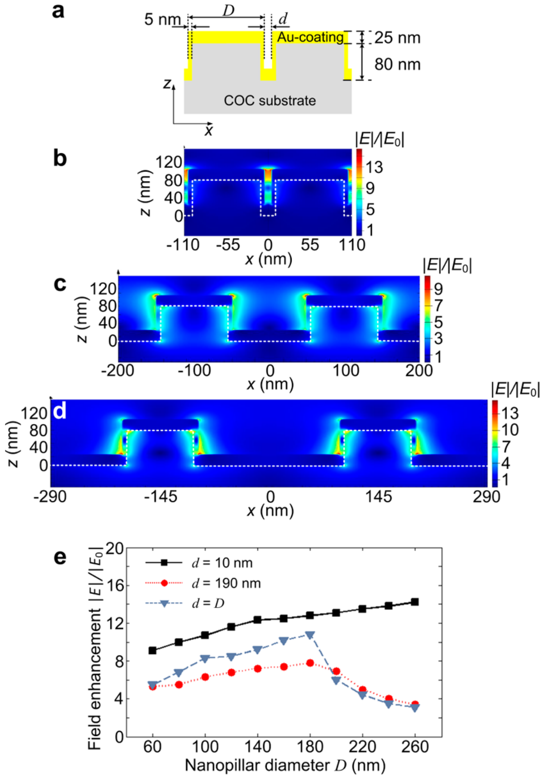

Figure 3. (a) Schematic side view of Au/COC nanopillars model for FDTD simulations. (b–d) Color-coded FDTD-simulated images of the near-field electric field intensity distributions for pairs of Au/COC nanopillars with diameter D = 100 nm and spacing d = 10, 100, and 190 nm, respectively. The dashed lines denote the COC nanopillar boundaries. z = 0 corresponds to the bottom of uncoated COC nanopillars. (e) FDTD-simulated electromagnetic field enhancement averaged over "hot spot" regions *versus* nanopillar diameter for three different nanopillar array patterns.

electric field regions were mainly confined within nanopillars (Figure S6 in Supporting Information) and practically did not contribute to the SERS effect. These trends are reflected in Figure 3e, which shows the average electric field enhancement in "hot spot" regions as a function of nanopillar diameter varying from 60 to 260 nm for three groups of arrays: having constant spacing of 10 and 190 nm and those with the spacing following the diameter (d = D). The "hot spot" region was defined as an area, where the enhanced electromagnetic field in the exterior of Au/COC nanopillars was no less than 1/e of the maximum value. Such a definition of the average electric field enhancement would appear to provide a more realistic estimation of the SERS effect than the maximum value. Another important factor determining the overall SERS efficiency is the relative "hot spot" area with regard to the whole SERS array area, as discussed in detail below.

The SERS effect of various Au/COC nanopillar arrays was first experimentally characterized using the laser dye rhodamine 6G (Rh6G) as the analyte (Rh6G deposits drop-cast from aqueous solution) and a helium—neon (He—Ne) laser as the excitation source at 632.8 nm. Figure 4a,b show SERS spectra of Rh6G molecules, which were acquired for different nanopillar arrays under the same experimental conditions. In accordance with the FDTD simulation results, the SERS signals of Rh6G exhibited a significant dependence on the nanopillar array geometry. In the case of arrays with the minimum interpillar spacing of d = 10 nm, the SERS intensity first increased with the increasing nanopillar diameter up to $D \sim 180$ nm, but then started to decrease for the larger diameter values, as seen in Figure 4a. For a set of arrays having nanopillar spacing equal to their diameter (d = D), the SERS intensity monotonically decreased with increasing diameter from 60 to 220 nm, as seen in Figure 4b. For comparison we performed similar measurements with commercially available Klarite SERS substrates (Renishaw Diagnostics). We found that the optimum nanopillar array patterns (*i.e.*, d = 10 nm, $D \sim 180$ nm) provided SERS signals which were stronger by a factor of ∼20 than those from Klarite SERS substrates. For evaluation of the absolute SERS enhancement factors (EFs), we compared the SERS response to the "standard" Raman signals of the analyte (Rh6G) taking into account the respective numbers of Rh6G molecules probed within the laser focus. In this comparison, the SERS signals are assumed to only arise from molecules occupying the calculated "hot spot" regions of a given SERS substrate. On the basis of our measurements and using the FDTD modeling estimation of the relative "hot spot" area, we evaluated the "hot spot" enhancement factor for the optimum nanopillar patterns to be about 10^7 (see Materials and Methods). Note that this value is about a factor of ∼200 higher than the EF calculated according to Equation 1 as the fourth power of the modeled electric field enhancement averaged over "hot spot" regions (average $|E|/|E_0| \sim 15$, as shown in Figure 3e). Such a discrepancy between the measured and calculated SERS EFs has often been seen and is usually attributed to the additional contribution of chemical effects not considered in the simulation.[47] One can also expect that the gold surface on the nanopillars is actually not as smooth as that of the model structures. Such surface roughness would lead to higher local electric field enhancements than predicted.

For nanopillar arrays with d = 10 nm, Figure 4c compares the experimental dependence of the SERS intensity (peak at 614 cm^{-1}, see Figure 4a) on array geometry (nanopillar diameter) with the calculated SERS "hot spot" average enhancement factors. The experimental intensity and calculated EFs are normalized to the values for the nanopillar array d = 10 nm, D = 60 nm and are shown in relative units. The measured SERS intensity increases more slowly than the calculated "hot spot" EFs and even slightly decreases for $D \geq 180$ nm. This discrepancy can be explained by the fact that, according to FDTD simulations, the relative area of the "hot spots" (*versus* the whole array area) decreases

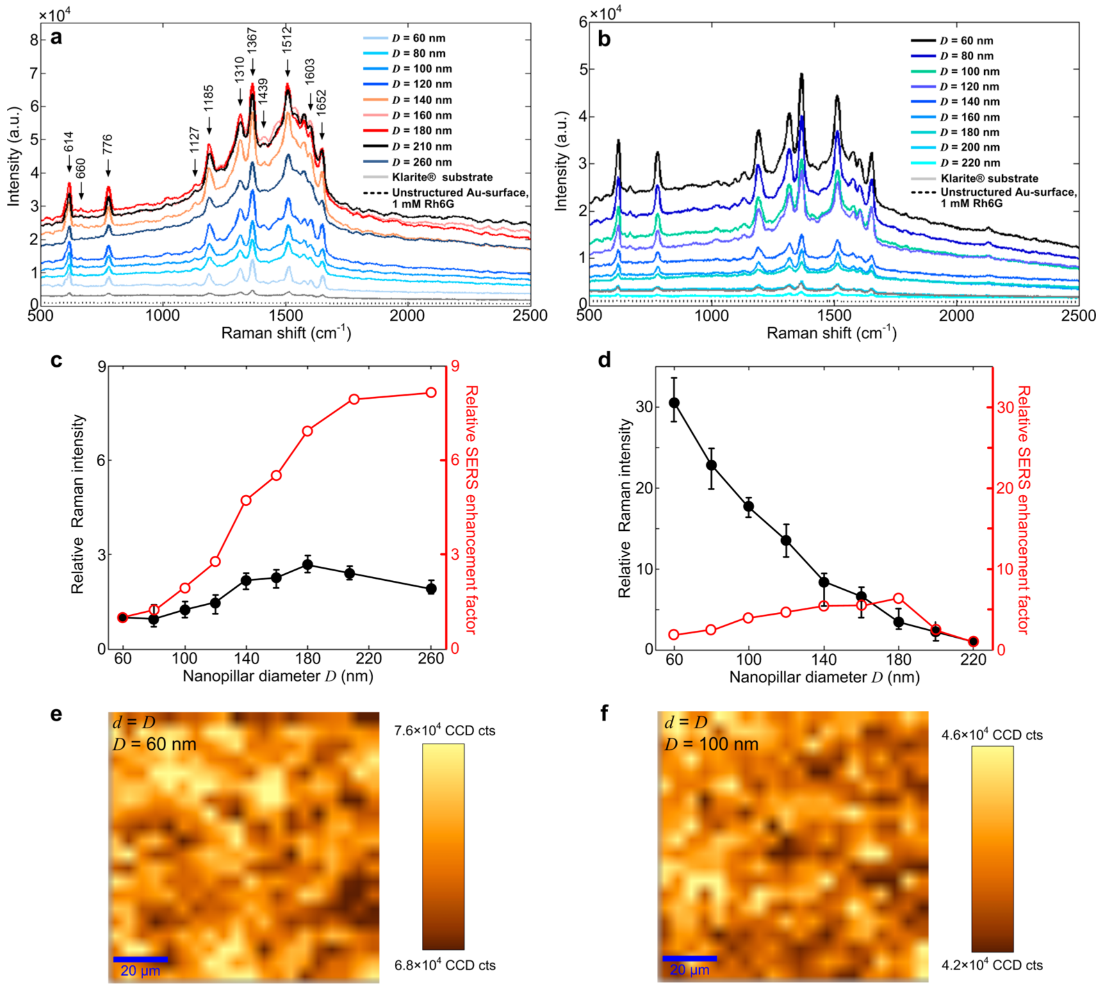

Figure 4. SERS spectra of Rh6G deposited on arrays with different nanopillar diameters D, and with interpillar spacings: (a) $d = 10$ nm and (b) d equals to D. Rh6G was deposited onto a 20 × 20 mm^2 multiarray substrate by drop-casting 30 μL of a 10 μM aqueous solution. The spectra (recorded after allowing the solutions to dry under ambient) are compared with those of Rh6G similarly deposited on a commercial Klarite SERS substrate and of a solid Rh6G layer deposited from a 1 mM solution onto an unstructured gold surface. All spectra were measured under the same conditions (4 mW excitation at 632.8 nm, 10 s acquisition time). Relative SERS signals and corresponding calculated "hot spot" average enhancement factors are shown as a function of nanopillar diameter for arrays with (c) $d = 10$ nm and (d) $d = D$, respectively. Typical SERS images of arrays with equal nanopillar spacing and diameter ($d = D$): (e) 60 nm and (f) 100 nm, respectively. The color-coded intensity corresponds to the area of the 614 cm^{-1} peak of Rh6G. Lateral resolution and pixel size are ∼2 μm and 2 × 2 μm^2, respectively.

upon increasing D. Correspondingly, fewer molecules would on average occupy the "hot spot" regions and thus contribute to the SERS signal (under the assumption of approximately uniform, nonsite-specific analyte deposition/adsorption onto the whole nanopillar array surface). According to simulations, the relative "hot spot" area is reduced by a factor of 4.3 by increasing D from 60 to 260 nm. Above $D \sim 180$ nm, the decrease of the "hot spot" area overweighs the increase of EF and the overall SERS efficiency starts to decrease.

The effect of the relative area of the "hot spot" regions can be further verified for the group of nanopillar arrays having equal nanopillar diameter and spacing ($d = D$), as shown in Figure 4d. The experimental results and calculated EFs are normalized to the values for the nanopillar array with $d = D = 220$ nm. The modeled EF in the "hot spots" rises relatively slowly when the nanopillar diameter increases in the range of $D \sim 60-180$ nm. Beyond $D \sim 180$ nm, the major enhancement of the electromagnetic field occurs only within nanopillars and the weakened coupling between nearby nanopillars results in a decrease of "hot spot" EFs. In parallel, the relative "hot spot" area diminishes strongly, even faster than in the case of $d = 10$ nm as discussed previously. Hence, the total SERS efficiency drops with increasing D. We conclude that the occupancy or relative area of the "hot spots" should not be neglected as it can play a significant role in determining the overall efficiency of a SERS substrate.

To characterize the lateral variation of the SERS response across nanopillar arrays, *i.e.*, the uniformity of the SERS substrates over length scales comparable to the laser focus, Raman images were acquired by *XY*-scanning the samples under a microscope objective with the aid of a piezo-stage. The scanned area and

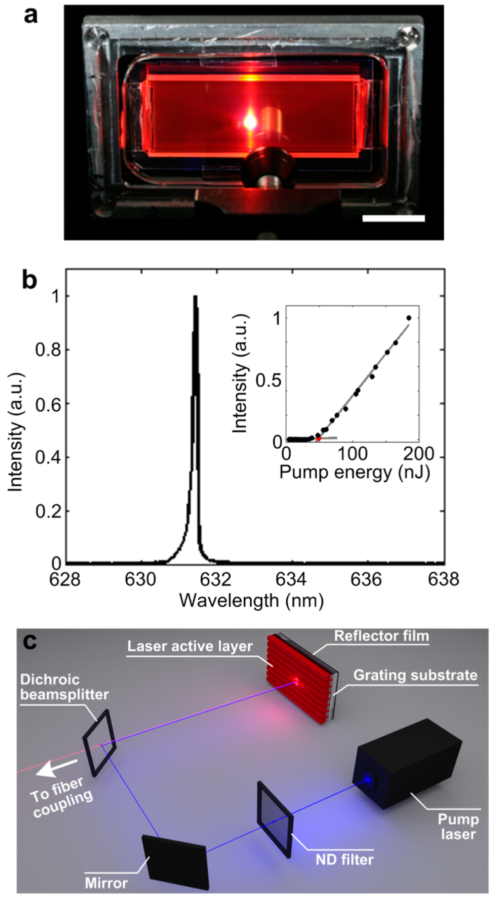

Figure 5. (a) Photograph of an encapsulated DFB-OSL when pumped by the UV laser. The scale bar corresponds to 1 cm. (b) Laser spectrum of the DFB-OSL fabricated with a homogeneous Alq_3:DCM active layer of 220 nm and input-output characteristic (inset) at the emission wavelength of 631.4 nm. (c) Schematic illustration of the organic laser module used as excitation source for SERS measurements.

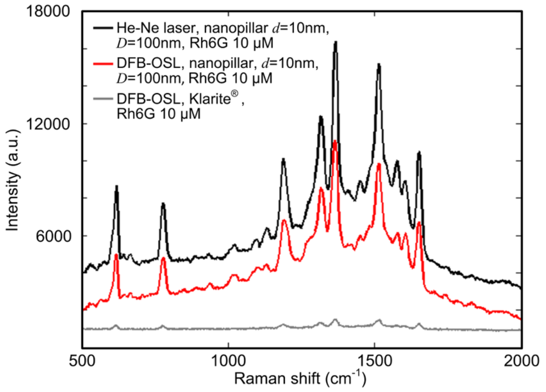

Figure 6. SERS spectra of Rh6G (drop-cast from 30 μL of a 10 μM aqueous solution) as measured on Au/COC nanopillar arrays (d = 10 nm, D = 100 nm), upon excitation with an organic semiconductor DFB laser and a He–Ne laser (both at 0.2 mW), in comparison with the Raman spectra of Rh6G on a Klarite SERS substrate (also drop-cast from 30 μL of a 10 μM aqueous solution). Measurement conditions: 20× objective, 600 g/mm grating, 5 s acquisition time.

lateral resolution were 0.1 × 0.1 mm^2 and ~2 μm (20× objective), respectively. Figure 4e,f show the color-coded images of the characteristic Raman peak of Rh6G at 614 cm^{-1} after subtraction of the broad background signal. Raman images acquired for several nanopillar arrays exhibited intensity variations in the SERS signals of less than 10%. This observation provides further evidence of the high accuracy and reproducibility of our laser-assisted replication process.

Recently, we have reported on the application of a DFB-OSL as a Raman excitation source in different instrument configurations, using both free-beam and fiber coupling.[22,23] Various organic active media have been applied in OSLs, which can cover practically the whole visible spectral range. In this work, in order to conform to the Raman microscope equipped with a He–Ne laser, we fabricated a DFB-OSL with a similar emission wavelength of 631.4 nm. This OSL was based on the efficient and stable Förster-energy-transfer blend of tris(8-hydroxyquinoline) aluminum (Alq_3) and the laser dye 4-(dicyanomethylene)-2-methyl-6-(*p*-dimethylaminostyryl)-4*H*-pyran (DCM) (for fabrication details see Materials and Methods and Figure S7 in Supporting Information). A photograph of the OSL in operation is presented in Figure 5a. The line width (spectral full width at half maximum) of the DFB-OSL device with a homogeneous active layer was 0.35 nm, when the UV pump power was set at 3.2 μJ $pulse^{-1}$ (see Figure 5b). The DFB-OSL exhibited a high slope efficiency of 6.8% and a laser threshold of 28 μJ cm^{-2} for a pump area of ~540 μm × 420 μm, as shown in the inset of Figure 5b. We utilized the bottom-emission from the DFB-OSL in addition to the surface-emission and thus almost doubled the power of the DFB-OSL in one direction up to ~0.6 mW. A dichroic beamsplitter was used to separate the organic laser and UV pump laser emissions, as shown in the scheme in Figure 5c.

In contrast to a standard He–Ne laser, the OSL is a quasi-continuous-wave Raman excitation source which emits short pulses (<1 ns) at a repetition rate of 10 kHz as determined by the DPSS UV-pump laser (Crylas, FTSS355-Q2). In addition, it generates an enlarged excitation spot on the sample in our setup (see Materials and Methods). However, these differences were proven unimportant for SERS detection. As illustrated in Figure 6 for Rh6G, similar Raman/SERS signals were detected using both lasers at the same excitation power.

Finally, we used our organic semiconductor DFB laser for the biomolecular SERS detection of adenosine deposited on one of the most efficient nanopillar arrays (d = 10 nm and D = 100 nm). Figure 7 shows the Raman spectra of adenosine molecules deposited by drop-casting from different aqueous solutions with concentrations ranging from 1 μM to 10 mM (using 30 μL volumes in each case). The detection limit for dried adenosine deposits prepared in this fashion was <300 pmol at the excitation power of 0.2 mW and relatively short acquisition time of 10 s. The sensitivity

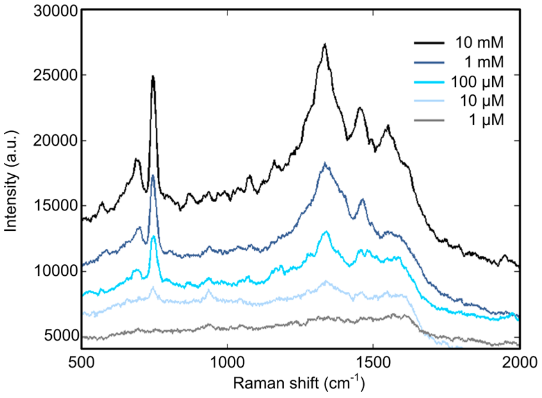

Figure 7. SERS spectra of adenosine deposited on Au/COC nanopillar arrays (d = 10 nm, D = 100 nm) from aqueous solutions with concentrations ranging from 1 μM to 10 mM (see text for details). SERS was excited with an organic semiconductor DFB laser at 631.4 nm at a power of 0.2 mW. Other measurement conditions: 20× objective lens, 600 g/mm grating and 10 s acquisition time.

is expected to be further improved by optimizing analyte deposition/adsorption as well as the optical detection scheme. Furthermore, dark-field scattering characterization and FDTD simulations (see Figure S4 in Supporting Information) predict that the spectral resonance peaks of some nanopillar arrays are slightly higher than our current laser wavelength. Consequently, the excitation at longer wavelengths (~750 nm and above) might be even more favorable. These nanoarrays may be of significant interest for NIR SERS analyses. We note that the NIR excitation range is currently practically inaccessible for organic semiconductor lasers (efficient lasing until ~700 nm). However, as the dense nanopillar arrays allow for the excitation of several modes in visible spectral range, it is promising to employ organic tunable lasers as excitation sources to study the excitation wavelength dependence in future.

CONCLUSIONS

In summary, laser-assisted replication has been used to fabricate SERS substrates consisting of arrays of gold-coated cyclic olefin copolymer nanopillars with variable diameters ranging from 60 to 260 nm. The spacing between adjacent nanopillars was precisely controlled down to ~10 nm. The employed silicon master templates were prepared by the standard lithography techniques and could be applied multiple times in the replication process. The replication is fast and potentially low-cost. We believe that this fabrication method may contribute to the advancement of analytical SERS applications. Furthermore, such polymer SERS substrates can be directly integrated into, *e.g.*, microfluidic or photonic devices. SERS enhancement factors estimated to be up to ~10^7 for Rh6G were determined for the "hot spot" regions in the nanopillar arrays, based on FDTD modeling of their lateral extent. The modeling also supported the experimentally characterized dependence of the SERS enhancement on the nanopillar array geometry (nanopillar diameter and spacing). In a first application of this approach, we have demonstrated the sensitive concentration detection of adenosine using replicated nanopillar arrays and an organic semiconductor DFB laser as the excitation source. This combination appears to be particularly promising for routine SERS biomolecular analytics in future miniaturized lab-on-a-chip devices.

MATERIALS AND METHODS

Fabrication of a Silicon Master Stamp. Poly(methyl methacrylate) (PMMA) 950k A2 (MicroChem) photoresist was spin-coated onto a 4″ silicon wafer for 60 s at 1250 rpm and subsequently baked on a hot plate at 180 °C for 5 min. Cylindrical nanowell patterns for later nanopillar arrays were written onto the photoresist across several discrete areas of 0.5 × 0.5 mm^2 using an electron beam (e-beam) writer (Vistec Lithography Inc., Vistec VB6). For three different silicon master stamps, the separation distance between adjacent nanowells was set at 20, 200 and ($D' + 20$) nm, respectively, where D' is the nanowell diameter. Each stamp contained 7 × 9 individual nanowell array sites. The line and column separation distances between these sites were defined as 1.5 and 2 mm, respectively. The nine lines corresponded to the sites with increasing nanowell diameter. The seven columns corresponded to applied e-beam doses (listed in Supporting Information), in order to optimize the e-beam writing and following etching process. After development with methyl isobutyl ketone and isopropyl alcohol (1:3) for 10 s, the photoresist structures were transferred into the silicon wafer by SF$_6$-based reactive ion etching. After stripping the PMMA resist, ~ 100 nm-deep nanowell arrays were exposed. An antiadhesion coating consisting of a self-assembled monolayer of fluorinated organosilanes finished the master stamp fabrication. To check array parameters such as nanowell diameters and separations, the stamp structures were further investigated *via* SEM and AFM. Supporting Information includes a schematic illustration of the fabrication process, photograph of one silicon template and typical SEM images (Figures S1, S2).

Dark-Field Scattering Characterization. Scattering intensity measurements were performed using scattering far-field detection *via* dark-field microscopy. The measurement setup is presented in Figure S3a in Supporting Information. A microscopy halogen lamp (Zeiss HAL 100) homogeneously illuminated a dark-field condenser (Zeiss, EC Epiplan NEOFLUAR, 50 × , NA = 0.8). The dark-field scattering from the nanostructures was then collected by the same objective and reflected onto an EMCCD camera (Andor) using an imaging spectrometer (Acton 2500i). The slit opening of the spectrometer was then used to selectively image lines of nanopillar arrays onto the EMCCD detector.

Finite-Difference-Time-Domain (FDTD) Simulations. We used the Lumerical FDTD Solutions program (version 8.7.4, www.lumerical.com) to perform our numerical calculations. To prevent numerical singularities in the form of electromagnetic "bursts" arising at the sharp edges and to take the realistic contours of our fabricated structures into account, the nanopillar edges were modeled by a curved surface with a radius of curvature of 3 nm. The boundaries of the simulation region in *x*, *y*-directions were set periodic to take the periodicity of the whole array into account. A 1 nm mesh in *x*, *y*, *z*-directions in the whole simulation region was found to be well suited for the convergence of the calculations. Figures S4–S6 (Supporting Information) show more details about FDTD simulations and related simulated images.

Raman Measurements. The SERS enhancement factor (EF) of Rh6G on Au/COC nanopillar arrays was estimated for the SERS peaks at 614 and 1367 cm^{-1} (shifted to 620 and 1381 cm^{-1}, respectively, for Rh6G in a reference aqueous solution dropped on a gold-coated unstructured COC substrate) using the following formula:[50]

$$\mathrm{EF} = \frac{I_{\mathrm{SERS}}/N_{\mathrm{surf}}}{I_{\mathrm{ref}}/N_{\mathrm{vol}}} \quad (2)$$

where I_{SERS} is the SERS intensity, N_{surf} is the number of molecules within the "hot spot" regions within the laser excitation spot, contributing to the measured SERS signal, I_{ref} is the non-SERS intensity from the reference sample, and N_{vol} is the number of molecules in the laser excitation/detection volume on the reference sample.

The laser excitation/detection volume was estimated as ~200 μm^3 for the microscope setup and objective (20×, NA = 0.4) applied. We applied 30 μL of a 10 mM Rh6G aqueous solution to a gold-coated unstructured COC substrate (reference sample). The total number of Rh6G molecules in this solution was about 1.8×10^{17}. For an excitation/detection volume of ~200 μm^3, N_{vol} was calculated as $\sim 1.2 \times 10^9$. Average signals I_{ref}(620 cm^{-1}) and I_{ref}(1381 cm^{-1}) were measured as 2290 and 4030 counts, respectively (5 mW excitation at 632.8 nm, 10 min acquisition time).

N_{surf} was calculated as the number of Rh6G molecules deposited in the "hot spot" regions of Au/COC nanopillars within the laser spot. These regions were defined from modeling as described above. For instance, for the Au/COC nanopillars with $d = 10$ nm and $D = 260$ nm, the "hot spot" area amounted to ~2000 nm^2 per nanopillar. Experimentally, a 10 nM diluted solution of Rh6G was applied and dried over the SERS substrate (20 × 20 mm^2). With regard to the very low analyte concentration (10 nM) applied, a roughly homogeneous, nonsite-specific analyte deposition/adsorption of the Rh6G molecules on the whole SERS substrate with Au/COC nanopillar arrays was assumed. Since the SERS areas (7 × 9 sites, each with a size of 0.5 × 0.5 mm^2) occupy only a small part of the whole substrate (20 × 20 mm^2), their contribution to the whole surface area is negligible. As a result, we approximate that the adsorbate density (per surface unit) is nearly the same for nanoarrays with different geometries. By depositing a 30 μL volume of a 10 nM diluted solution, this corresponded to about 4.5×10^{-4} molecules/nm^2. Within one laser excitation spot (diameter of ~4 μm), there are about 150 nanopillars with $d = 10$ nm and $D = 260$ nm. The number of molecules within the "hot spot" regions N_{surf} is about 140. The SERS measurement results showed I_{SERS}(614 cm^{-1}) = 2990 counts and I_{SERS}(1367 cm^{-1}) = 4670 counts (5 mW excitation at 632.8 nm, 10 min acquisition time). Hence, the SERS enhancement factors are EF(614 cm^{-1}) $\approx 1 \times 10^7$ and EF(1367 cm^{-1}) $\approx 9 \times 10^6$. We note that, in general, different vibrational modes can be associated with different SERS enhancement factors.[51−53] This effect has typically been attributed to a specific orientation of analyte molecules or to their interaction with a SERS substrate.[53−55] In our case, this effect for Rh6G is apparently not significant.

Fabrication and Operation of the Organic Semiconductor DFB Laser. The organic semiconductor tris(8-hydroxyquinoline) aluminum ($\mathrm{Alq_3}$) doped with the laser dye 4-(dicyanomethylene)-2-methyl-6-(*p*-dimethylaminostyryl)-4*H*-pyran (DCM) forms a very efficient and stable Förster energy transfer system with a red emitting spectra range and was chosen as the active gain material for our laser devices. The fabrication process is shown in Figure S7. To match this red emitter, we applied a glass substrate with one-dimensional corrugation with a period of 400 nm (Visolas GmbH) as the second-order DFB resonator. $\mathrm{Alq_3}$ and DCM (2.8 wt %) were thermally coevaporated in a high vacuum chamber, forming a film with a thickness of 220 nm on the grating substrate. The laser device was subsequently encapsulated by bonding a glass lid with an ultraviolet (UV) curable optical adhesive (Norland, NOA68), in order to prevent photodegradation when exposed to air.

In this work, we conveniently used the DFB-OSL as an external, quasi-CW Raman excitation source, which was pumped at 10 kHz with a nanosecond-pulsed DPSS laser at 355 nm (Crylas, FTSS355-Q2). The output power of the OSL was ~0.6 mW. It was contributed both by the bottom and surface emission from the active layer. This was achieved by adding a reflector film (3M, Vikuiti Enhanced Specular Reflector ESR) on the bottom of the DFB grating substrate. The present lifetime of the DFB-OSL is sufficient for proof-of-principle measurements but needs to be improved for routine analytics. Corresponding laser degradation was followed by monitoring the output power while maintaining the pump pulse energy and frequency constant. Typically, laser power decayed by only 10% within the first 30 min of operation at the above pumping conditions. Such stability is sufficient for typical SERS measurements of up to a few minutes. Note that the initial DFB-OSL power can be completely recovered by slightly moving the pump spot to another active layer position. Due to insufficient confinement in the grating orientation, the DFB-OSL also operates on higher-order transverse modes. Correspondingly, a multimode optical fiber with a core diameter of 50 μm had to be used to efficiently couple (~70%) the OSL beam and transfer it to the microscope in the fiber-coupling scheme. The overall efficiency of light transfer from the OSL to a given sample was determined to be 40%. Correspondingly, samples were exposed to a maximum excitation power of 0.25 mW. Because of the multimode fiber coupling, the OSL produced a significantly larger excitation spot on the sample (~20 μm with a 20× objective) as compared with a standard He−Ne laser (coupled *via* a single-mode fiber). The image of this spot as produced by a tube lens in the Raman microscope was also correspondingly enlarged. To efficiently collect Raman light over this enlarged area, while keeping the spectral resolution almost unchanged, we employed a round-to-line fiber bundle (LightGuide Optics, L2000) for coupling the microscope exit (tube lens focal point) to a spectrograph. The line output of the fiber bundle was oriented to correspond to the entrance slit of the spectrograph.

Conflict of Interest: The authors declare no competing financial interest.

Acknowledgment. The authors thank R. Hünig for fruitful discussions, A. Bacher, P.-J. Jakobs and A. Muslija for the silicon template fabrication and P. Abaffy for taking SEM images. This work was supported by the Deutsche Forschungsgemeinschaft and the State of Baden-Württemberg through the DFG-Center for Functional Nanostructures (CFN). The work of X. L. is supported by Carl-Zeiss-Stiftung and Karlsruhe School of Optics & Photonics (KSOP). We acknowledge support by Deutsche Forschungsgemeinschaft and Open Access Publishing Fund of Karlsruhe Institute of Technology. Finally, the support for laser processing by the Karlsruhe Nano Micro Facility (KNMF, http://www.knmf.kit.edu), a Helmholtz research infrastructure at the Karlsruhe Institute of Technology, is gratefully acknowledged.

Supporting Information Available: Supplementary details about the fabrication of silicon master stamps and the organic semiconductor DFB laser, further FDTD simulation results. This material is available free of charge *via* the Internet at http://pubs.acs.org.

REFERENCES AND NOTES

1. Pelletier, M. J., Ed.; *Analytical Applications of Raman Spectroscopy*; Blackwell Science: Oxford, 1999; pp 1−52.
2. Weber, W. H.; Merlin, R., Eds.; *Raman Scattering in Materials Science*; Springer: Berlin, 2000; pp 1−26.
3. Salzer, R.; Siesler, H. W., Eds.; *Infrared and Raman Spectroscopic Imaging*; Wiley VCH: Weinheim, 2009; pp 1−60.
4. Nabiev, I.; Chourpa, I.; Manfait, M. Applications of Raman and Surface-Enhanced Raman Scattering Spectroscopy in Medicine. *J. Raman Spectrosc.* **1994**, *25*, 13–23.
5. Choo-Smith, L.-P.; Edwards, H. G. M.; Endtz, H. P.; Kros, J. M.; Heule, F.; Barr, H.; Robinson, J. S., Jr.; Bruining, H. A.; Puppels, G. J. Medical Applications of Raman Spectroscopy: From Proof of Principle to Clinical Implementation. *Biopolymers* **2002**, *67*, 1–9.
6. Mak, J. S. W.; Rutledge, S. A.; Abu-Ghazalah, R. M.; Eftekhari, F.; Irizar, J.; Tam, N. C. M.; Zheng, G.; Helmy, A. S. Recent

Developments in Optofluidic-Assisted Raman Spectroscopy. *Prog. Quant. Electron.* **2013**, *37*, 1–50.

7. Liu, G. L.; Lee, L. P. Nanowell Surface Enhanced Raman Scattering Arrays Fabricated by Soft-Lithography for Label-Free Biomolecular Detections in Integrated Microfluidics. *Appl. Phys. Lett.* **2005**, *87*, 074101.
8. Lim, C.; Hong, J.; Chung, B. G.; deMello, A. J.; Choo, J. Optofluidic Platforms Based on Surface-Enhanced Raman Scattering. *Analyst* **2010**, *135*, 837–844.
9. Dochow, S.; Beleites, C.; Henkel, T.; Mayer, G.; Albert, J.; Clement, J.; Krafft, C.; Popp, J. Quartz Microfluidic Chip for Tumour Cell Identification by Raman Spectroscopy in Combination with Optical Traps. *Anal. Bioanal. Chem.* **2013**, *405*, 2743–2746.
10. Dochow, S.; Becker, M.; Spittel, R.; Beleites, C.; Stanca, S.; Latka, I.; Schuster, K.; Kobelke, K.; Unger, S.; Henkel, T.; *et al.* Raman-on-Chip Device and Detection Fibres with Fibre Bragg Grating for Analysis of Solutions and Particles. *Lab Chip* **2013**, *13*, 1109–1113.
11. Tessler, N.; Denton, G. J.; Friend, R. H. Lasing from Conjugated-Polymer Microcavities. *Nature* **1996**, *382*, 695–697.
12. Hide, F.; DiazGarcia, M. A.; Schwartz, B. J.; Andersson, M. R.; Pei, Q. B.; Heeger, A. J. A New Class of Solid-State Laser Materials. *Science* **1996**, *273*, 1833–1836.
13. Frolov, S. V.; Ozaki, M.; Gellermann, W.; Vardeny, Z. V.; Yoshino, K. Mirrorless Lasing in Conducting Polymer Poly-(2,5-dioctyloxy-p-phenylenevinylene) Films. *Jpn. J. Appl. Phys.* **1996**, *35*, L1371–L1373.
14. Klinkhammer, S.; Woggon, T.; Geyer, U.; Vannahme, C.; Dehm, S.; Mappes, T.; Lemmer, U. A Continuously Tunable Low-Threshold Organic Semiconductor Distributed Feedback Laser Fabricated by Rotating Shadow Mask Evaporation. *Appl. Phys. B: Laser Opt.* **2009**, *97*, 787–791.
15. Klinkhammer, S.; Liu, X.; Huska, H.; Shen, Y.; Vanderheiden, S.; Valouch, S.; Vannahme, C.; Bräse, S.; Mappes, T.; Lemmer, U. Continuously Tunable Solution-Processed Organic Semiconductor DFB Lasers Pumped by Laser Diode. *Opt. Express* **2012**, *20*, 6357–6364.
16. Herrnsdorf, J.; Wang, Y.; Mckendry, J. J. D.; Gong, Z.; Massoubre, D.; Guilhabert, B.; Tsiminis, G.; Turnbull, G. A.; Samuel, I. D. W.; Laurand, N.; *et al.* Micro-LED Pumped Polymer Laser: A Discussion of Future Pump Sources for Organic Lasers. *Laser Photonics Rev.* **2013**, *7*, 1065–1078.
17. Vannahme, C.; Klinkhammer, S.; Kolew, A.; Jakobs, P.-J.; Guttmann, M.; Dehm, S.; Lemmer, U.; Mappes, T. Integration of Organic Semiconductor Lasers and Single-Mode Passive Waveguides into a PMMA Substrate. *Microelectron. Eng.* **2010**, *87*, 693–695.
18. Liu, X.; Klinkhammer, S.; Sudau, K.; Mechau, N.; Vannahme, C.; Kaschke, J.; Mappes, T.; Wegener, M.; Lemmer, U. Ink-Jet-Printed Organic Semiconductor Distributed Feedback Laser. *Appl. Phys. Express* **2012**, *5*, 072101.
19. Oki, Y.; Miyamoto, S.; Maeda, M.; Vasa, N. J. Multiwavelength Distributed-Feedback Dye Laser Array and its Application to Spectroscopy. *Opt. Lett.* **2002**, *27*, 1220–1222.
20. Woggon, T.; Klinkhammer, S.; Lemmer, U. Compact Spectroscopy System Based on Tunable Organic Semiconductor Lasers. *Appl. Phys. B: Laser Opt.* **2010**, *99*, 47–51.
21. Klinkhammer, S.; Woggon, T.; Vannahme, C.; Mappes, T.; Lemmer, U. Optical Spectroscopy with Organic Semiconductor Lasers. *Proc. SPIE* **2010**, *7722*, 77221I.
22. Liu, X.; Stefanou, P.; Wang, B.; Woggon, T.; Mappes, T.; Lemmer, U. Organic Semiconductor Distributed Feedback (DFB) Laser as Excitation Source in Raman Spectroscopy. *Opt. Express* **2013**, *21*, 28941–28947.
23. Liu, X.; Lebedkin, S.; Mappes, T.; Köber, S.; Koos, C.; Kappes, M.; Lemmer, U. Organic Semiconductor Distributed Feedback Laser as Excitation Source in Raman Spectroscopy using Free-Beam and Fibre Coupling. *Proc. SPIE* **2014**, *9137*, 91370Y.
24. Lyon, L. A.; Keating, C. D.; Fox, A. P.; Baker, B. E.; He, L.; Nicewarner, S. R.; Mulvaney, S. P.; Natan, M. J. Raman Spectroscopy. *Anal. Chem.* **1998**, *70*, 341–361.
25. Kneipp, K.; Kneipp, H.; Itzkan, I.; Dasari, R. R.; Feld, M. S. Surface-Enhanced Raman Scattering and Biophysics. *J. Phys.: Condens. Matter* **2002**, *14*, R597–R624.
26. Leem, J.; Kang, H. W.; Ko, S. H.; Sung, H. J. Controllable Ag Nanostructure Patterning in a Microfluidic Channel for Real-Time SERS Systems. *Nanoscale* **2014**, *6*, 2895–2901.
27. Aroca, R. F.; Alvarez-Puebla, R. A.; Pieczonka, N.; Sanchez-Cortez, S.; Ramos, J. V. Surface-Enhanced Raman Scattering on Colloidal Nanostructures. *Adv. Colloid Interface Sci.* **2005**, *116*, 45–61.
28. Brown, R. J. C.; Wang, J.; Tantra, R.; Yardley, R. E.; Milton, M. J. T. Electromagnetic Modelling of Raman Enhancement from Nanoscale Substrates: A Route to Estimation of the Magnitude of the Chemical Enhancement Mechanism in SERS. *Faraday Discuss.* **2006**, *132*, 201–213.
29. Ochsenkühn, M. A.; Jess, P. R. T.; Stoquert, H.; Dholakia, K.; Campbell, C. J. Nanoshells for Surface-Enhanced Raman Spectroscopy in Eukaryotic Cells: Cellular Response and Sensor Development. *ACS Nano* **2009**, *3*, 3613–3621.
30. Khoury, C. G.; Vo-Dinh, T. Gold Nanostars For Surface-Enhanced Raman Scattering: Synthesis, Characterization and Optimization. *J. Phys. Chem. C* **2008**, *112*, 18849–18859.
31. Mulvihill, M. J.; Ling, X. Y.; Henzie, J.; Yang, P. Anisotropic Etching of Silver Nanoparticles for Plasmonic Structures Capable of Single-Particle SERS. *J. Am. Chem. Soc.* **2010**, *132*, 268–274.
32. Etchegoin, P. G.; Le Ru, E. C. A Perspective on Single Molecule SERS: Current Status and Future Challenges. *Phys. Chem. Chem. Phys.* **2008**, *10*, 6079–6089.
33. Tantra, R.; Brown, R. J. C.; Milton, M. J. T. Strategy to Improve the Reproducibility of Colloidal SERS. *J. Raman Spectrosc.* **2007**, *38*, 1469–1479.
34. Hulteen, J. C.; Van Duyne, R. P. Nanosphere Lithography: A Materials General Fabrication Process for Periodic Particle Array Surfaces. *J. Vac. Sci. Technol. A* **1995**, *13*, 1553–1558.
35. Chaney, S. B.; Shanmukh, S.; Dluhy, R. A.; Zhao, Y.-P. Aligned Silver Nanorod Arrays Produce High Sensitibity Surface-Enhanced Raman Spectroscopy Substrates. *Appl. Phys. Lett.* **2005**, *87*, 031908.
36. Brown, R. J. C.; Milton, M. J. T. Nanostructures and Nanostructured Substrates for Surface-Enhanced Raman Scattering (SERS). *J. Raman Spectrosc.* **2008**, *39*, 1313–1326.
37. Felidj, N.; Truong, S. L.; Aubard, J.; Levi, G.; Krenn, J. R.; Hohenau, A.; Leitner, A.; Aussenegg, F. R. Gold Particle Interaction in Regular Arrays Probed by Surface Enhanced Raman Scattering. *J. Chem. Phys.* **2004**, *120*, 7141–7146.
38. Green, M.; Liu, F. M. J. SERS Substrates Fabricated by Island Lithography: The Silver/Pyridine System. *J. Phys. Chem. B* **2003**, *107*, 13015–13021.
39. Huang, J.-A.; Zhao, Y.-Q.; Zhang, X.-J.; He, L.-F.; Wong, T.-L.; Chui, Y.-S.; Zhang, W.-J.; Lee, S.-T. Ordered Ag/Si Nanowires Array: Wide-Range Surface-Enhanced Raman Spectroscopy for Reproducible Biomolecule Detection. *Nano Lett.* **2013**, *13*, 5039–5045.
40. Choi, C. J.; Xu, Z.; Wu, H.-Y.; Liu, G. L.; Cunningham, B. T. Surface-Enhanced Raman Nanodomes. *Nanotechnology* **2010**, *21*, 415301.
41. Abu Hatab, N. A.; Oran, J. M.; Sepaniak, M. J. Surface-Enhanced Raman Spectroscopy Substrates Created *via* Electron Beam Lithography and Nanotransfer Printing. *ACS Nano* **2008**, *2*, 377–385.
42. Wu, W.; Hu, M.; Ou, F. S.; Li, Z.; Williams, R. S. Cones Fabricated by 3D Nanoimprint Lithography for Highly Sensitive Surface Enhanced Raman Spectroscopy. *Nanotechnology* **2010**, *21*, 255502.
43. Sahoo, P. K.; Vogelsang, K.; Schift, H.; Solak, H. H. Surface Plasmon Resonance in Near-Field Coupled Gold Cylinder Arrays Fabricated by EUV-Interference Lithography and Hot Embossing. *Appl. Surf. Sci.* **2009**, *256*, 431–434.
44. Wissmann, M.; Besser, H.; Beiser, M.; Pfleging, W. Laser Moulding, a New Low-Cost Fabrication Process for Micro- and Nanostructured Components. *Microsyst. Technol.* **2014**, 10.1007/s00542-014-2227-3.

45. Goyal, S.; Thorson, M. R.; Schneider, C. L.; Zhang, G. G. Z.; Gong, Y.; Kenis, P. J. A. A Microfluidic Platform for Evaporation-based Salt Screening of Pharmaceutical Parent Compounds. *Lab Chip* **2013**, *13*, 1708–1723.
46. Pallikari, F.; Chondrokoukis, G.; Rebelakis, M.; Kotsalas, Y. Raman spectroscopy: A Technique for Estimating Extent of Polymerization in PMMA. *Mater. Res. Innovations* **2001**, *4*, 89–92.
47. Stiles, P. L.; Dieringer, J. A.; Shah, N. C.; Van Duyne, R. P. Surface-Enhanced Raman Spectroscopy. *Annu. Rev. Anal. Chem.* **2008**, *1*, 601–626.
48. Kneipp, K. Surface-Enhanced Raman Scattering. *Phys. Today* **2007**, *60*, 40–46.
49. Wissert, M. D.; Schell, A. W.; Ilin, K. S.; Siegel, M.; Eisler, H.-J. Nanoengineering and Characterization of Gold Dipole Nanoantennas with Enhanced Integrated Scattering Properties. *Nanotechnology* **2009**, *20*, 425203.
50. Le Ru, E. C.; Blackie, E.; Meyer, M.; Etchegoin, P. G. Surface Enhanced Raman Scattering Enhancement Factors: A Comprehensive Study. *J. Phys. Chem. C* **2007**, *111*, 13794–13803.
51. Moskovits, M. Surface Selection Rules. *J. Chem. Phys.* **1982**, *77*, 4408–4416.
52. Creighton, J. A. The Effective Raman Tensor for SER Scattering by Molecules Adsorbed at the Surface of a Spherical Particle. *Surf. Sci.* **1985**, *158*, 211–221.
53. Persson, B. N. J. On the Theory of Surface-Enhanced Raman Scattering. *Chem. Phys. Lett.* **1981**, *82*, 561–565.
54. Saikin, S. K.; Chu, Y.; Rappoport, D.; Crozier, K. B.; Aspuru-Guzik, A. Separation of Electromagnetic and Chemical Contributions to Surface-Enhanced Raman Spectra on Nanoengineered Plasmonic Substrates. *J. Phys. Chem. Lett.* **2010**, *1*, 2740–2746.
55. Alonso-Gonzalez, P.; Albella, P.; Schnell, M.; Chen, J.; Huth, F.; Garcia-Etxarri, A.; Casanova, F.; Golmar, F.; Arzubiaga, L.; Hueso, L. E.; *et al.* Resolving the Electromagnetic Mechanism of Surface-Enhanced Light Scattering at Single Hot Spots. *Nat. Commun.* **2012**, *3*, 684.